



Direct growth of Fe-incorporated NiSe microspheres on FeNi alloy foam as a highly efficient electrocatalyst for oxygen evolution reaction

Li Zhang^{1,2} · Peng Yang¹ · Wanjun Chen¹ · Long Cheng¹ · Jianhui Yan¹ · Haihua Yang^{1,2} 

Received: 8 April 2020 / Accepted: 3 August 2020 / Published online: 11 August 2020
© Springer Science+Business Media, LLC, part of Springer Nature 2020

Abstract

Transition metal selenides with special structures and rational component modulation have received tremendous research interest to ameliorate the sluggish kinetics of oxygen evolution reaction (OER) in electrochemical water splitting. Here, we propose a facile hydrothermal treatment strategy to prepare porous Fe-incorporated NiSe microspheres via in situ selenization of iron–nickel foam. The as-obtained 3D integrated anode demonstrates excellent electrocatalytic performance towards OER in concentrated alkaline media (1.0 M KOH), with a small onset overpotential of 170 mV, an overpotential as low as 236 mV to achieve a current density of 50 mA cm⁻², and a small Tafel slope of 53 mV dec⁻¹. The overpotential at 50 mA cm⁻² shows no obvious change during the whole durability test for 24 h, indicating long-term stable electrocatalytic activity. Characterizations of the electrode after stability test reveal the oxidation of the crystallized Fe-incorporated NiSe microspheres which probably generates amorphous Ni(Fe)OOH. The microspheres were partially dissolved and connected with each other to form a wormlike porous structure. The superior OER activity is largely attributed to the highly active Fe–Ni selenide and derived oxyhydroxide of 3D porous structure on the FeNi foam substrate. The facile synthesis strategy in this work can be conveniently applied to the preparation of a variety of selenides of metal foams with different compositions as highly efficient electrocatalysts.

1 Introduction

The depletion of traditional fossil fuels and the deterioration of the environment have prompted people to seek clean, efficient, and safe alternative energy sources. In this regard, great attention has been paid to the development of new energy sources, especially hydrogen as a research hotspot of renewable energy [1, 2]. As a carbon-free and abundant energy resource, hydrogen has been massively produced by electrocatalytic water splitting [3–5]. Because of the impedance of solution, electrode, etc., a practical voltage much higher than the theoretical voltage of water electrolysis is required to carry out the electrolysis process. The

electrocatalytic water splitting involves the cathode hydrogen evolution reaction (HER) and the anode oxygen evolution reaction (OER), in which two electrons are involved in the formation of hydrogen molecules, while four electrons are involved in the formation of oxygen molecules. The process of anode OER is more complex than that of the cathode HER, so the overpotential of anode OER is higher than that of cathode HER under the same conditions. Because of its sluggish kinetics, the anode OER has been taken as the bottleneck in electrocatalytic water splitting, and high overpotentials are required [6, 7]. Designing high-performance OER catalysts offers a feasible way to reduce the overpotential and boost the overall efficiency. Although precious metal oxides, such as IrO₂ and RuO₂, are considered as the most efficient benchmarked OER catalysts, the high cost and scarcity impede their large-scale application [8, 9].

In the past decades, numerous efforts have been made to explore earth-abundant and high-performance OER catalysts [10, 11]. The earth-abundant transition metals (such as iron, cobalt, copper, and especially nickel) and their related compounds, including oxides [12–16], hydroxides [17, 18], sulfides [19, 20], selenides [21–25], phosphides [26–28], have been proven to be promising alternatives to the precious

✉ Haihua Yang
hhyang@126.com

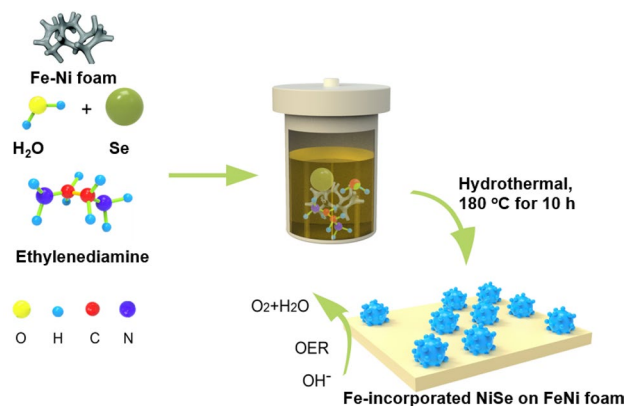
¹ School of Chemistry and Chemical Engineering, Hunan Institute of Science and Technology, Yueyang 414006, Hunan, People's Republic of China

² Key Laboratory of Hunan Province for Advanced Carbon-Based Functional Materials, Hunan Institute of Science and Technology, Yueyang 414006, Hunan, People's Republic of China

metal oxides. It has been reported recently that the electrocatalytic performance of nickel oxides or hydroxides can be greatly improved by Fe doping or incorporation [29–31]. It is believed that more catalytic active sites can be generated upon Fe doping or incorporation to change the electronic structure of Ni-related active sites. Additionally, Fe doping or incorporation can also enhance the conductivity and offer synergistic effect between Fe and Ni metals. Inspired by this strategy, Fe–Ni-based sulfides [32, 33], phosphides [34, 35], and selenides [36–38] have been designed and reported for electrocatalytic water splitting.

Typically, various metal selenides have been readily prepared by different methods with high-active surface, which benefit to the OER activity. Xu et al. reported the iron–nickel–selenide (Fe–Ni–Se) nanorods fabricated by one-pot solvothermal selenization process. The Fe–Ni–Se nanorods grown on nickel foam current collectors exhibit outstanding oxygen evolution reaction activity with a remarkably low overpotential of 290 mV at 60 mA cm^{-2} [39]. Coupling these active catalysts with three-dimensional (3D) porous conductive current collectors (Ni foam [38–41], carbon fiber cloth [36, 37], etc.) to construct integrated electrodes leads to further improvement of OER activity. The support of nickel–iron selenides on these substrates was usually achieved by two steps, including initial hydrothermal treatment of externally added Fe and Ni ions to grown Fe–Ni hydroxide precursors on the substrates, which were subsequently converted to selenides via hydrothermal or solvothermal process. Besides Ni foam, FeNi alloy foam has also emerged as good support and current collect for OER electrocatalysts [42–44]. Recently, Sun et al. demonstrated the development of Fe-doped rhombohedral NiSe nanoflakes array on FeNi foam as high-active OER electrocatalysts, which required an onset overpotential as low as 200 mV in 1.0 M KOH [45]. It should be noted that the electrocatalytic activity is closely related to the crystal structures and morphologies, which can be controlled by synthesis methods and procedures. It would be interesting to prepare FeNi foam-based selenides with special structures and morphologies which are expected to serve as highly efficient OER catalysts.

With these perspectives, we herein actualized direct growth of Fe-incorporated NiSe microspheres on FeNi alloy foam by a facile one-pot hydrothermal reaction (Scheme 1). Compared to the previously reported fabrication methods, our synthesis process possesses the unique features that FeNi alloy foam was employed as both substrate and Fe–Ni sources without adding external Fe and Ni metal ions, and selenium powder was directly used as Se source without the formation of any precursors. The as-obtained 3D-integrated OER anode exhibited high electrocatalytic activity towards OER in concentrated alkaline solution (1 M KOH), showing a small onset overpotential of 170 mV, a low overpotential



Scheme 1 Schematic illustration of the in situ growth process of Fe-incorporated NiSe microspheres on FeNi foam

of 236 mV to achieve a current density of 50 mA cm^{-2} , and a small Tafel slope of 53 mV dec^{-1} . The overpotential at 50 mA cm^{-2} showed no obvious change during the whole stability test for 24 h. The excellent OER performance is largely attributed to the active Fe–Ni-based compounds with 3D porous structure.

2 Experimental

2.1 Preparation of Fe-incorporated NiSe microspheres on FeNi alloy foam

The reagents were of analytical grade and employed as received without further purification. FeNi alloy foam was purchased from Kunshan Jiayisheng electronic materials Co. Ltd. Fe-incorporated NiSe microspheres were grown on FeNi alloy foam via a one-step hydrothermal process (Scheme 1). A piece of FeNi foam ($1 \text{ cm} \times 1.5 \text{ cm}$) was immersed in 3.0 M HCl solution for 30 min to remove the possible oxide layer on the surface, and ultrasonically cleaned with DI water, acetone, and ethanol for several times. 0.5 mmol of selenium powder was ultrasonically dispersed in the mixture of ethylenediamine (25 ml) and DI water (15 ml). The mixture and the clean FeNi foam were transferred and sealed in a Teflon-lined stainless steel autoclave, and heated at 180 °C for 10 h. After naturally cooling down, the sample was washed with DI water for several times, and then dried in a vacuum oven at 60 °C for 6 h to obtain Fe-incorporated NiSe microspheres on FeNi alloy foam (denoted as Fe–NiSe@FeNi foam) with microspheres mass loading of $\sim 12 \text{ mg cm}^{-2}$.

2.2 Characterization

X-ray diffraction (XRD) of the as-obtained samples were characterized by a D/max- γ B X-ray diffractometer (Rigaku, Japan) with $\text{CuK}\alpha$ radiation ($\lambda = 1.54178 \text{ \AA}$). The surface elemental chemical states were investigated by X-ray photoelectron spectroscopy (XPS, ESCALAB 250Xi, USA) with reference to the C 1s peak at 284.8 eV. The morphologies and nanostructures were probed by scanning electron microscope (FEI Nova Nano SEM 230, USA), transmission electron microscope (TEM,) and high-resolution transmission electron microscope (HRTEM, Model JEOL-2100, Japan). The Brunauer–Emmett–Teller (BET)-specific surface area was determined using a nitrogen adsorption isotherm apparatus (ST-08 analyzer).

2.3 Electrochemical measurements

The electrochemical tests of the samples were performed with CHI 660E electrochemical workstation (Chenhua, Shanghai, China) in a standard three-electrode electrochemical cell using Fe–NiSe@FeNi foam, Pt plate, and saturated calomel electrode (SCE) as working electrode, counter electrode, and reference electrode, respectively. All electrochemical measurements were carried out in an electrolyte of 1 M KOH (pH 13.7). The potentials in this paper were calibrated with respect to the reversible hydrogen electrode (RHE) by using the equation $E(\text{RHE}) = E(\text{SCE}) + 1.07 \text{ V}$. Linear sweep voltammograms (LSV) with iR correction

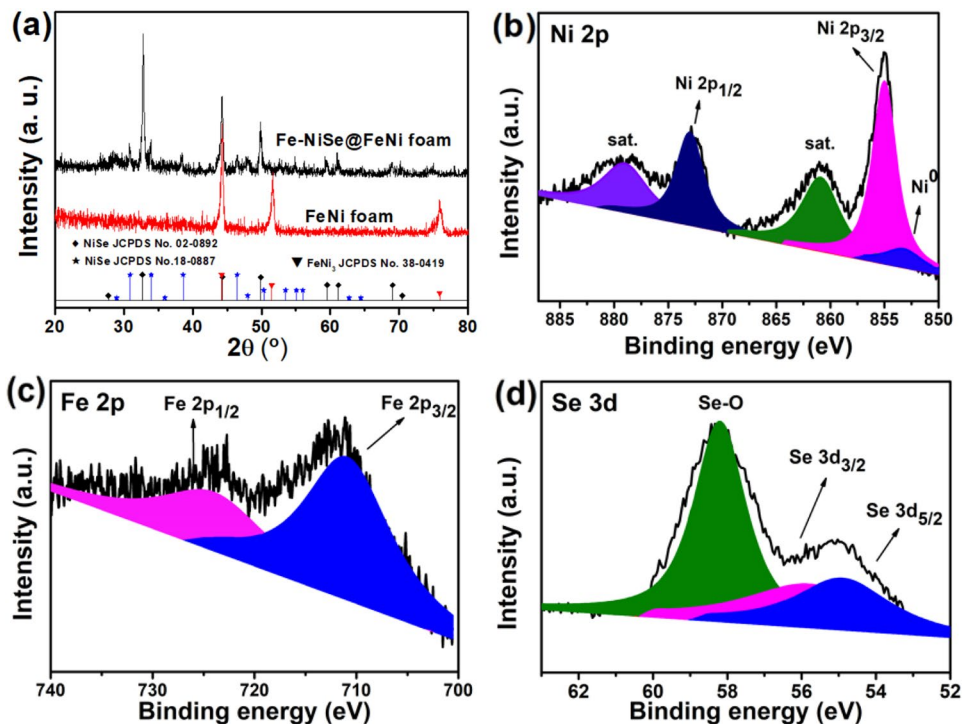
were conducted with a scan rate of 5 mV s^{-1} . The electrochemical impedance spectroscopy (EIS) tests were measured in the frequency range of 100 kHz to 0.01 Hz at 1.6 V vs. RHE with an AC perturbation of 5 mV. The stability of Fe–NiSe@FeNi foam electrode was evaluated by Chronopotentiometry under a constant current density of 50 mA cm^{-2} for 24 h to record the potential change.

3 Results and discussion

The schematic illustration of the in situ growth process of Fe-incorporated NiSe microspheres on FeNi foam is shown in Scheme 1. Porous Fe-incorporated NiSe microspheres were successfully prepared by direct reaction between iron–nickel foam and selenium powder via a facile one-step hydrothermal process. The FeNi alloy foam acted as both substrate and Fe and Ni sources, and selenium powder was directly used as Se source without formation of any precursors.

The XRD patterns of bare FeNi foam and Fe–NiSe@FeNi foam are displayed in Fig. 1a. The diffraction peaks of bare FeNi foam match well with the FeNi_3 alloy of cubic phase (JCPDS No. 38-0419) [30, 45]. After hydrothermal treatment, additional diffraction peaks belong to hexagonal NiSe (JCPDS No. 02-0892) and rhombohedral mackininite NiSe (JCPDS No. 18-0887) were observed without any other impurities [38, 45]. The peaks located at $2\theta = 27.85^\circ, 32.77^\circ, 44.36^\circ, 49.93^\circ, 59.55^\circ, 61.16^\circ, 69.05^\circ,$ and 70.41° can be

Fig. 1 a XRD patterns of bare FeNi foam and Fe–NiSe@FeNi foam. High-resolution Ni 2p (b), Fe 2p (c), and Se 3d (d) XPS spectra for Fe–NiSe@FeNi foam



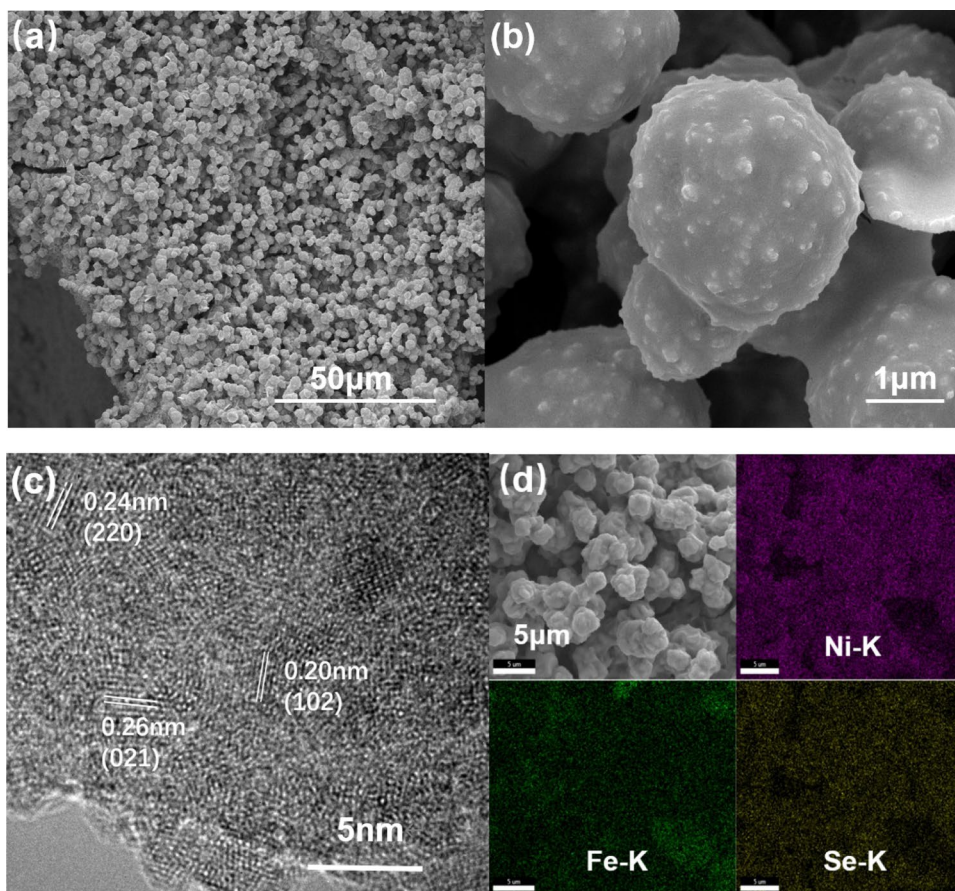
assigned to the (100), (101), (102), (110), (103), (201), (202), and (004) planes of NiSe (JCPDS No. 02-0892). Besides the NiSe (JCPDS No. 02-0892) peaks, a few peaks were also observed at $2\theta = 29.06^\circ$, 31.02° , 34.06° , 36.04° , 38.69° , 46.53° , 48.04° , 50.37° , 53.54° , 55.11° , 56.02° , 62.72° , and 64.42° well matched with the (101), (300), (021), (220), (211), (131), (410), (401), (321), (330), (012), (122), and (600) planes of NiSe (JCPDS No. 18-0887). No diffraction peak of Fe-related compounds was detected, which may be due to the consistent substitution of Fe for Ni because of their similar atomic sizes [38, 39].

XPS was carried out to characterize the surface composition and valence states of the Fe–NiSe microspheres. As shown in the high-resolution XPS spectrum of Ni 2p (Fig. 1b), the fitted low peak at 852.8 eV is attributed to metallic Ni from the FeNi foam, and the two peaks of Ni 2p_{1/2} at 873.1 eV and Ni 2p_{3/2} at 855.5 eV with two shakeup satellites confirming the Ni²⁺ state in the sample [45]. The peak located at 852.5 eV is assigned to Ni⁰ 2p_{1/2}. The peaks of Fe 2p_{1/2} at 724.8 eV and Fe 2p_{3/2} at 711.4 eV in Fig. 1c indicate the existence of Fe³⁺, while no satellite peaks belonging to Fe₂O₃ were discovered [29, 45], further suggesting that Fe³⁺ ions were incorporated into NiSe. The fitted peaks of Se 3d at 54.9 and 55.8 eV in Fig. 1d are

representative of Se 3d_{5/2} and Se 3d_{3/2}, respectively [36]. The broad peak at 58.3 eV is assigned to Se–O bond because of the surface oxidation of the sample. Both the XRD and XPS results confirm that the Fe³⁺ ions are incorporated into NiSe lattice.

To obtain the morphology and microstructure of the as-prepared Fe–NiSe@FeNi foam, SEM was carried out. The SEM images (Fig. 2a, b) of the as-obtained Fe–NiSe@FeNi foam indicate that the surface of the FeNi foam is fully covered by packed porous Fe-incorporated NiSe microspheres with diameter of ca. 3 μm. It should be noted that the 3D structure of the FeNi foam has been retained after in situ selenization. The enlarged SEM image (Fig. 2b) presents rough microsphere surface, which consist of a large number of small particles, indicating more exposure of surface area. As proved by BET test, the specific area and pore volume of FeNi foam are greatly increased from 2.1 and 0.003 cm³ g^{−1} to 3.2 and 0.006 cm³ g^{−1}, respectively, after the formation of Fe–NiSe@FeNi foam. The rough and porous structure of the Fe-incorporated NiSe microspheres can better realize the optimization of desirable properties, which can provide abundant active sites, effectively increase the electrolyte contact, and decrease transfer pathways of electrons. To further investigate the Fe-incorporated NiSe, the TEM

Fig. 2 SEM images (a, b), HRTEM image (c), and EDX elemental mapping (d) of the as-synthesized Fe–NiSe@FeNi foam



images of Fe–NiSe microspheres detached ultrasonically from the Fe–Ni foam substrate and dispersion in ethanol. HRTEM image of the microsphere (Fig. 2c) shows clear lattice fringes with interplanar spaces of 0.24 and 0.26 nm assigned to the (220) and (021) planes of makinenite NiSe (JCPDS No. 18-0887), and the lattice spacing of 0.20 nm indexed to the (102) plane of hexagonal NiSe (JCPDS No. 02-0892). EDX elemental mapping image (Fig. 2d) of the microspheres depicts well-distributed Ni, Fe, and Se elements. The EDX mapping confirms that the corresponding elements are homogeneously distributed on the microsphere, and the atomic percent of Fe is determined to be 18%. These results further verify the successful construction of Fe-incorporated NiSe microspheres.

The electrocatalytic OER activity of Fe–NiSe@FeNi foam as a 3D electrode was investigated (Fig. 3) in alkaline aqueous electrolyte (1 M KOH, Ph 13.7) with Pt plate and SCE electrode as the counter electrode and reference electrode, respectively. For comparison, bare FeNi foam and commercial RuO₂ on FeNi foam with a mass loading of ~12 mg cm⁻² were also tested under the same conditions. LSV curves of these electrodes were first probed as shown in Fig. 3a. It shows that the commercial RuO₂ on FeNi foam reveals an expected overpotential (η_{10}) of 256 mV at the current density of 10 mA cm⁻², close to the value of 280 mV as reported [46]. The bare FeNi foam also behaved as efficient OER catalyst similar to previous report [43], delivering overpotentials of 347, 388, and 403 mV to reach 10, 50, and 100 mA cm⁻², respectively. Impressively, the

OER performance of FeNi foam was greatly enhanced after in situ selenization, and the Fe–NiSe@FeNi foam electrode required much lower overpotentials of 197, 236, and 266 mV to drive 10, 50, and 100 mA cm⁻², respectively.

As the kinetics parameter for OER, the Tafel slope was calculated by plotting overpotential against log(J) base on the equation $\eta = b \log J + a$. As depicted in Fig. 3b, the Tafel slope of 53 mV dec⁻¹ for Fe–NiSe@FeNi foam is comparable with that of 57 mV dec⁻¹ for RuO₂ and 56 mV dec⁻¹ for bare FeNi foam, suggesting good OER kinetics for FeNi foam-based electrodes. The overpotentials at different current densities and Tafel slope of Fe–NiSe@FeNi foam electrode in this work and some other reported FeNi foam-related electrodes are summarized in Table 1. All the Fe–Ni samples demonstrate considerable OER activity, especially for the Fe-incorporated NiSe microspheres@FeNi foam electrode in this work.

As we know, the OER performance is closely related to the charge transfer resistance (R_{ct}). As shown in Fig. 3c, the EIS results were fitted with the equivalent circuit. The Fe–NiSe@FeNi foam reveals the smallest R_{ct} value of 1.198 Ω among these catalysts, which means that the short charge transfer length and efficient charge transfer, namely, the favorable charge transfer kinetics, intrinsically electrical conductivity and the incorporated Fe may exert charge transfer activation on NiSe. As derived from the Nyquist plots in Fig. 3c, both bare FeNi foam electrode, RuO₂@FeNi foam, and Fe–NiSe@FeNi foam electrode possess small electrolyte solution resistance (R_s), which might be attributed to the

Fig. 3 LSV curves (a), Tafel slope curves (b), Nyquist plots at 1.6 V vs. RHE with an equivalent circuit (c) and capacitive current density (d) of bare FeNi foam, Fe–NiSe@FeNi foam and RuO₂@FeNi foam

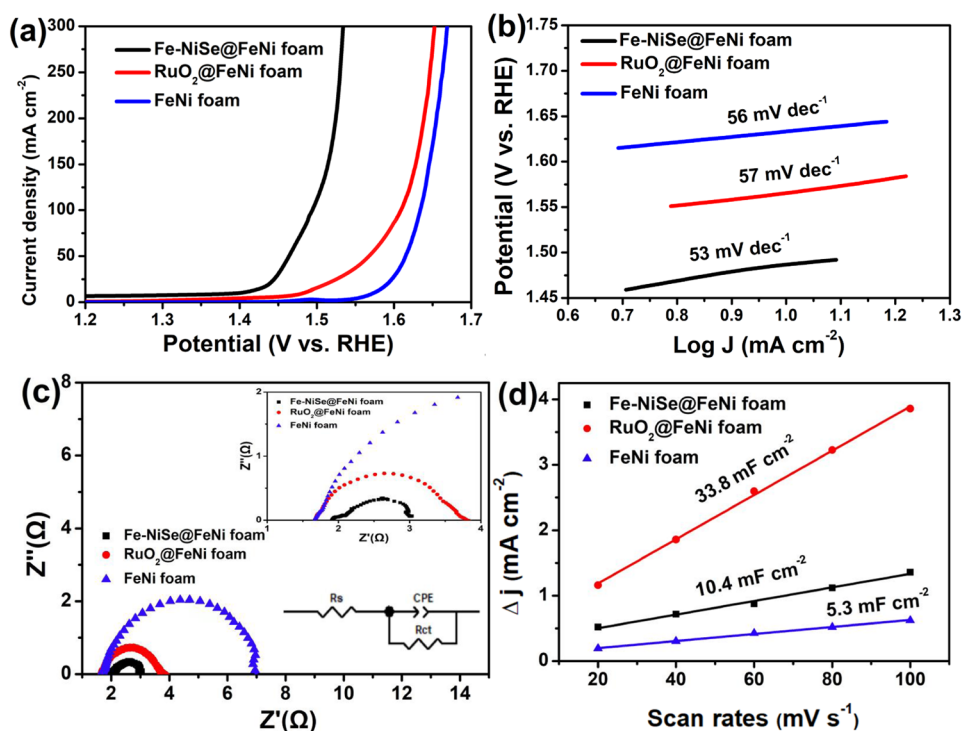


Table 1 Comparison of the OER activities of FeNi-related electrocatalysts in 1 M KOH

Catalyst	η_0 (mV)	η_{10} (mV)	η_{50} (mV)	η_{100} (mV)	Tafel slope (mV dec ⁻¹)	Refs
NiFe phosphate/phosphide@NiFe foam	/	230	/	/	57	[47]
Redox sculptured NiFe foam	/	245	/	294	38	[48]
Rose-like Ni–Fe selenide@Ni foam	/	197	/	/	56	[38]
Ni–Fe selenide nanorods@Ni foam	/	/	/	290 (η_{60})	61	[39]
Ni _{0.5} Fe _{0.5} Se ₂ nanosheets@carbon fiber cloth	270	/	/	/	63	[37]
Ni _{0.75} Fe _{0.25} Se ₂ nanosheets@carbon fiber cloth	/	/	255 (η_{35})	277	47	[36]
Ni _x Fe _{1-x} Se ₂ -derived oxide@Ni foam	/	195	/	/	28	[21]
Fe-doped NiSe nanoflakes@FeNi foam	200	/	245	264	65	[45]
Fe-incorporated NiSe microspheres@FeNi foam	170	197	236	266	53	This work

3D porous structure of FeNi foam for facilitating the interfacial electron transfer between the electrocatalyst and the electrolyte. The electrochemical active surface area (ECSA) was determined by measuring the cyclic voltammetry (CV) curves in the double-layer region at various scan rates. Figure 3d shows the electrochemical double-layer capacitance (C_{dl}) as the representation of the ECSA to evaluate the OER activity of the catalysts. The calculated electrochemical double-layer capacitances (C_{dl}) of Fe–NiSe@FeNi foam, RuO₂@FeNi foam, and FeNi foam are 10.4 mF cm⁻², 33.8 mF cm⁻², and 5.3 mF cm⁻², respectively. The largest C_{dl} observed for RuO₂@FeNi foam implies that it possesses the highest ECSA. It is worth noting that the C_{dl} of Fe–NiSe@FeNi foam is 1.96 times that of bare FeNi foam, demonstrating that the active sites can be largely increased with Fe-incorporated NiSe microspheres in situ grown and embedded in FeNi foam substrate, which is consistent with the BET results.

Besides the efficient performance, the long-term stability is another important criterion to be reckoned with for practical application. The durability of Fe–NiSe@FeNi foam electrode was assessed by chronopotentiometric measurement at a fixed current density of 50 mA cm⁻² over 24 h. The chronopotentiometric curve in Fig. 4a shows that the potential remained stable during the whole assessment. The LSV curves were also recorded before and after the

chronopotentiometric measurement (Fig. 4b). Although a slight decay of activity was observed for Fe–NiSe@FeNi foam electrode after chronopotentiometric measurement, the electrocatalyst still showed excellent OER activity. The anodic peak at around 1.46 V vs. RHE is ascribed to the oxidation reaction of Ni²⁺ to Ni³⁺ [36].

In order to get insight into the OER reaction mechanism, XRD, SEM, and XPS techniques were employed to elucidate the structure and composition change of the Fe–NiSe@FeNi foam after chronopotentiometric measurement (Fig. 5). As presented in Fig. 5a, the Fe-incorporated NiSe microspheres were partially dissolved and connected with each other to form wormlike porous structure. The XRD pattern of the Fe–NiSe@FeNi foam after chronopotentiometric measurement (Fig. 5b) is almost the same as that for the bare FeNi foam, suggesting that the crystallized Fe-incorporated NiSe microspheres were converted to amorphous wormlike layer. The above situation may be attributed to the irreversible phase transition of metal selenides to metal oxides or oxyhydroxide caused by strong anodic oxidation. The high-resolution XPS spectrum of Ni 2p (Fig. 5c) displays a peak at 857 eV, which can be assigned to the Ni³⁺ state because of the formation of nickel oxyhydroxide (NiOOH) [36, 45]. The dominant peak of Se–O bond and the nearly eliminated Se 3d peaks in Fig. 5d further confirm the oxidation of crystallized Fe-incorporated NiSe and the formation

Fig. 4 Chronopotentiometric curve of Fe–NiSe@FeNi foam electrode at a fixed current density of 50 mA cm⁻² (a), and LSV curves before and after the chronopotentiometric measurement (b)

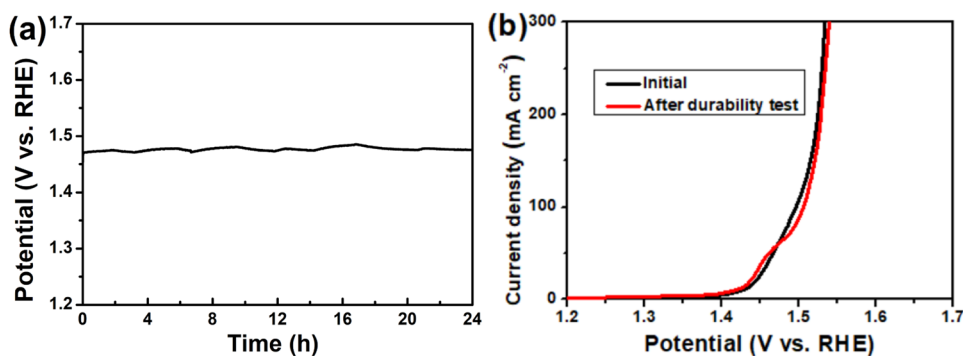
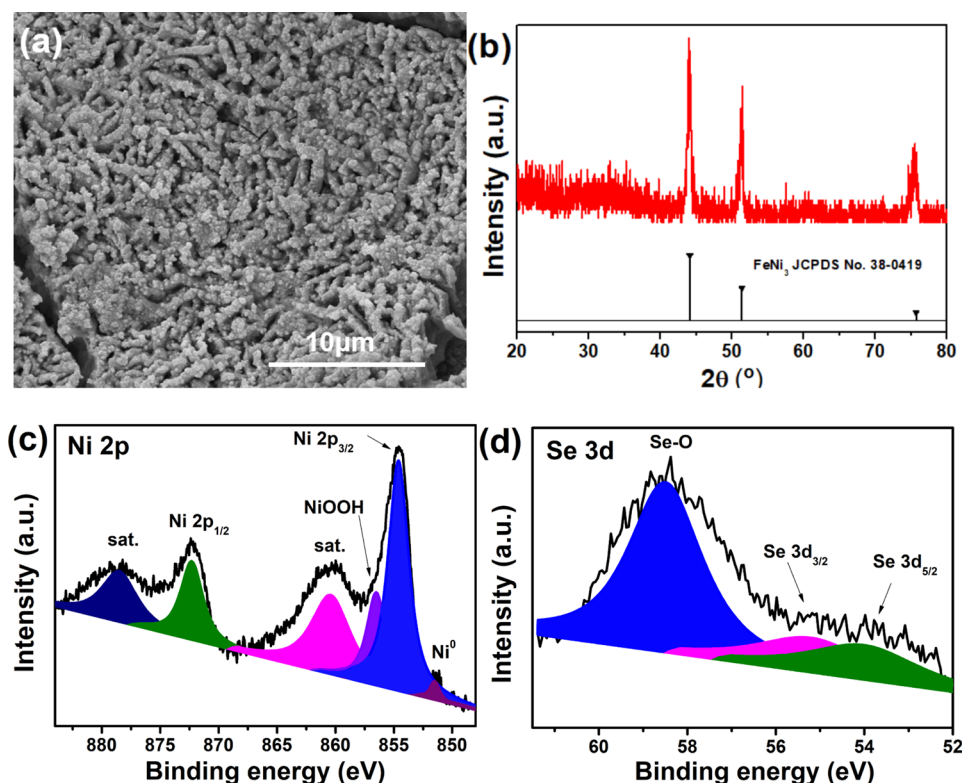


Fig. 5 SEM image (a), XRD pattern (b), and high-resolution Ni 2p (c) and Se 3d (d) XPS spectra for Fe–NiSe@FeNi foam after the stability test



of Ni(Fe)OOH. These phenomena are consistent with other Fe–Ni-related catalysts in the previous reports [21, 36, 45]. Based on the above information, it has been demonstrated that both Fe–Ni selenide and oxyhydroxide are responsible for the high electrocatalytic activity from the initial evaluation throughout the whole stability test. Furthermore, by combining the porous Fe-incorporated NiSe microspheres or wormlike Ni(Fe)OOH with the 3D porous FeNi foam substrate, the integrated electrode can offer large pore volume and high specific area for exposing more effective active site, and facilitate the electrolyte penetrating and contacting with the active sites on the nanoparticles. It is worth noting that the rough structure of the microspheres can maximize the exposure active area. At the same time, due to the similar lattice structure of iron and nickel, the incorporation of iron can contribute a part of the charge transfer activity on NiSe, which can not only enhance the conductivity, but also generate a large number of active edge sites. The synergistic effect is exerted between Fe-incorporated NiSe and Fe–Ni matrix.

4 Conclusions

In summary, Fe-incorporated NiSe microspheres were successfully prepared by in situ selenization of iron–nickel foam via a facile one-step hydrothermal process. This 3D porous electrode exhibits outstanding OER activity in concentrated alkaline media, delivering low overpotentials of 197 mV

at 10 mA cm^{-2} , 236 mV at 50 mA cm^{-2} , and 266 mV at 100 mA cm^{-2} , as well as a small Tafel slope of 53 mV dec^{-1} . Impressively, the OER activity has been maintained during the stability test, even though the crystallized Fe-incorporated NiSe transformed to amorphous worm-like Ni(Fe)OOH. The excellent OER performance may be attributed to the integration of 3D porous FeNi foam substrate with the high-active Fe-incorporated NiSe microspheres or wormlike Ni(Fe)OOH, which are propitious to offer large pore volume and high specific area for exposing more effective active site, and accelerate the electrolyte penetrating and electrons transport. This work not only provides an excellent OER catalyst, but also potentially paves the way to the preparation of metal foams selenides derived compounds with different compositions as eco-friendly and efficient electrocatalysts.

Acknowledgements This work was financially supported by the Innovation Platform Foundation Project of Hunan Education Department of China (No. 18K087), the Natural Science Foundation for Youths of Hunan Province of China (No. 2019JJ50206), and the Scientific Research Project of Hunan Education Department of China (No.19B230).

References

1. A. Landman, H. Dotan, G.E. Shter, M. Wullenkord, A. Houaijia, A. Maljusch, G.S. Grader, A. Rothschild, *Nat. Mater.* **16**, 646 (2017)
2. J.A. Turner, *Science* **305**, 972 (2004)

3. J. Yeston, *Science* **355**, 143 (2017)
4. G.W. Crabtree, M.S. Dresselhaus, M.V. Buchanan, *Phys. Today* **57**, 39 (2004)
5. C.C.L. McCrory, S. Jung, J.C. Peters, T.F. Jaramillo, *J. Am. Chem. Soc.* **135**, 16977 (2013)
6. H. Dau, C. Limberg, T. Reier, M. Risch, S. Roggan, P. Strasser, *ChemCatChem* **2**, 724 (2010)
7. N.-T. Suen, S.-F. Hung, Q. Quan, N. Zhang, Y.-J. Xu, H.M. Chen, *Chem. Soc. Rev.* **46**, 337 (2017)
8. E. Willinger, C. Massué, R. Schlögl, M.G. Willinger, *J. Am. Chem. Soc.* **139**, 12093 (2017)
9. H. Over, *Chem. Rev.* **112**, 3356 (2012)
10. X. Zou, Y. Zhang, *Chem. Soc. Rev.* **44**, 5148 (2015)
11. J. Li, Y. Wang, T. Zhou, H. Zhang, X. Sun, J. Tang, L. Zhang, A.M. Al-Enizi, Z. Yang, G. Zheng, *J. Am. Chem. Soc.* **137**, 14305 (2015)
12. Y. Li, P. Hasin, Y. Wu, *Adv. Mater.* **22**, 1926 (2010)
13. L. Zhang, Q. Liang, P. Yang, Y. Huang, W. Chen, X. Deng, H. Yang, J. Yan, Y. Liu, *Int. J. Hydrogen Energ.* **44**, 24209 (2019)
14. K. Wang, C. Liu, W. Wang, N. Mitsuzaki, Z. Chen, *J. Mater. Sci. Mater. Electron.* **30**, 4144 (2019)
15. C. Liu, K. Wang, J. Zhang, X. Zheng, Q. Liang, Z. Chen, *J. Mater. Sci. Mater. Electron.* **29**, 10744 (2018)
16. Y. Li, Z. Zhou, H. Xu, X. Liao, G. Cheng, M. Sun, L. Yu, *J. Mater. Sci. Mater. Electron.* **30**, 18424 (2019)
17. C. Hao, H. Linfeng, C. Min, Y. Yan, W. Limin, *Adv. Funct. Mater.* **24**, 934 (2014)
18. S. Chen, J. Duan, M. Jaroniec, S.Z. Qiao, *Angew. Chem. Int. Edit.* **52**, 13567 (2013)
19. S. Arumugam, G. Pandian, S. Sangaraju, *Adv. Funct. Mater.* **26**, 4661 (2016)
20. J. Tie, S. Peng, G. Diao, F. Chen, M. Sun, L. Yu, J. Zhou, Y. Li, *J. Mater. Sci. Mater. Electron.* **29**, 2251 (2018)
21. X. Xu, F. Song, X. Hu, *Nat. Commun.* **7**, 12324 (2016)
22. X. Shi, H. Wang, P. Kannan, J. Ding, S. Ji, F. Liu, H. Gai, R. Wang, *J. Mater. Chem. A* **7**, 3344 (2019)
23. X. Wang, B. Zheng, B. Yu, B. Wang, W. Hou, W. Zhang, Y. Chen, *J. Mater. Chem. A* **6**, 7842 (2018)
24. C. Liu, K. Wang, X. Zheng, X. Liu, Q. Liang, Z. Chen, *Carbon* **139**, 1 (2018)
25. M. Zhuang, Y. Ding, X. Ou, Z. Luo, *Nanoscale* **9**, 4652 (2017)
26. G. Chen, T. Ma, Z. Liu, N. Li, Y. Su, K. Davey, S. Qiao, *Adv. Funct. Mater.* **26**, 3314 (2016)
27. L. Marc, K.C. Sandra, P. Christian, S. Hans-Peter, A. Markus, S. Menny, *Angew. Chem. Int. Edit.* **54**, 12361 (2015)
28. C.Y. Son, I.H. Kwak, Y.R. Lim, J. Park, *Chem. Commun.* **52**, 2819 (2016)
29. K. Fominykh, P. Chernev, I. Zaharieva, J. Sicklinger, G. Stefanic, M. Döblinger, A. Müller, A. Pokharel, S. Böcklein, C. Scheu, T. Bein, D. Fattakhova-Rohlfing, *ACS Nano* **9**, 5180 (2015)
30. J. Xie, H. Qu, F. Lei, X. Peng, W. Liu, L. Gao, P. Hao, G. Cui, B. Tang, *J. Mater. Chem. A* **6**, 16121 (2018)
31. J. Wang, X. Teng, Y. Niu, L. Guo, J. Kong, X. He, Z. Chen, *RSC Adv.* **9**, 21679 (2019)
32. P. Ganesan, A. Sivanantham, S. Shanmugam, *J. Mater. Chem. A* **4**, 16394 (2016)
33. S. Qin, J. Lei, Y. Xiong, X. Xu, X. Geng, J. Wang, *RSC Adv.* **9**, 10231 (2019)
34. Z. Ma, R. Li, M. Wang, H. Meng, F. Zhang, X.-Q. Bao, B. Tang, X. Wang, *Electrochim. Acta* **219**, 194 (2016)
35. F. Hu, H. Wang, Y. Zhang, X. Shen, G. Zhang, Y. Pan, J.T. Miller, K. Wang, S. Zhu, X. Yang, C. Wang, X. Wu, Y. Xiong, Z. Peng, *Small* **15**, 1901020 (2019)
36. Z. Wang, J. Li, X. Tian, X. Wang, Y. Yu, K.A. Owusu, L. He, L. Mai, *A.C.S. Appl. Mater. Inter.* **8**, 19386 (2016)
37. J.-Q. Chi, X. Shang, F. Liang, B. Dong, X. Li, Y.-R. Liu, K.-L. Yan, W.-K. Gao, Y.-M. Chai, C.-G. Liu, *Appl. Surf. Sci.* **401**, 17 (2017)
38. J. Yu, G. Cheng, W. Luo, *Nano Res.* **11**, 2149 (2018)
39. J. Du, A. Yu, Z. Zou, C. Xu, *Inorg. Chem. Front.* **5**, 814 (2018)
40. W. Tang, S. Zuo, J. Wang, Y. Mi, Z. Chen, *Electrochim. Acta* **247**, 835 (2017)
41. Y.-Y. Sun, M.-Y. Jiang, L.-K. Wu, G.-Y. Hou, Y.-P. Tang, M. Liu, *Sustain. Energy Fuels* **4**, 582 (2020)
42. C. Cao, D.-D. Ma, Q. Xu, X.-T. Wu, Q.-L. Zhu, *Adv. Funct. Mater.* **29**, 1807418 (2019)
43. Y. Liang, Q. Liu, A.M. Asiri, X. Sun, Y. He, *Int. J. Hydrogen Energ.* **40**, 13258 (2015)
44. X. Bu, R. Wei, W. Gao, C. Lan, J.C. Ho, *J. Mater. Chem. A* **7**, 12325 (2019)
45. C. Tang, A.M. Asiri, X. Sun, *Chem. Commun.* **52**, 4529 (2016)
46. A. Li, C. Wang, H. Zhang, Z. Zhao, J. Wang, M. Cheng, H. Zhao, J. Wang, M. Wu, J. Wang, *Electrochim. Acta* **276**, 153 (2018)
47. Q. Zhang, T. Li, J. Liang, N. Wang, X. Kong, J. Wang, H. Qian, Y. Zhou, F. Liu, C. Wei, Y. Zhao, X. Zhang, *J. Mater. Chem. A* **6**, 7509 (2018)
48. Y. Wu, R. Su, Y. Li, Z. Wang, Z. Lü, L. Xu, B. Wei, *Electrochim. Acta* **309**, 415 (2019)

Publisher's Note Springer Nature remains neutral with regard to jurisdictional claims in published maps and institutional affiliations.